Magnetic-Driven Swimming Microrobots

JINGFAN CHEN[a], HANWEN HU[a] and YA WANG[a,b,c,*]

[a]J. Mike Walker ‘66 Department of Mechanical Engineering, Texas A&M University, College Station, TX 77843
[b]Department of Electrical and Computer Engineering, Texas A&M University, College Station, TX, 77843
[c]Department of Biomedical Engineering, Texas A&M University, College Station, TX, 77843
[d]Department of Computer Science and Engineering
[*]Corresponding Authors. E-mail addresses: ya.wang@tamu.edu (Ya Wang)

Abstract:

A magnetic object subject to an external rotating magnetic field would be rotated due to the alignment tendency between its internal magnetization and the field. Based on this principle, 12 shapes of swimming microrobots around 1mm long were designed and 3D-printed using biodegradable materials Poly (ethylene glycol) diacrylate (PEDGA). Their surface was decorated with superparamagnetic iron oxide nanoparticles (SPIO NPs) to provide magnetic responsivity. An array of 12 permanent magnets generated a rotating uniform magnetic field (~ 100 mT) to impose magnetic torque, which induces a tumbling motion in the microrobot. We developed a dynamic model that captured the behavior of swimming microrobots of different shapes and showed good agreement with experimental results. Among these 12 shapes, we found that microrobots with equal length, width, and depth performed better. The observed translational speed of the Hollow Cube microrobot can exceed 17.84 mm/s (17.84 body lengths/s) under a rotating magnetic field of 5.26 Hz. These microrobots could swim to the targeted sites in a simplified vessel branch. And a finite element model was created to simulate the motion of the swimming microrobot under a flow rate of 0.062 m/s.

1. Introduction

Microrobots, like microorganisms, transport in a low Reynolds number regime, requiring motion patterns that differ from macroscale animals. According to Purcell's scallop theorem[1], nonreciprocal motion is necessary to obtain net movement or displacement in low Reynolds number Newtonian fluids, in which viscous forces dominate compared to inertial forces. Wireless magnetic-driven microrobots have drawn extensive attention due to their potential for minimally invasive medical operations [2-4]. These microrobots are rationally designed to execute a variety of tasks, such as drug delivery[5, 6] and sensing and diagnosis [7] by simulating the locomotion systems of microorganisms and forming their motion types under magnetic stimulation (for example, cork-screw forward by rotating magnetic field [8, 9], translation by magnetic field gradients[10], fluctuation by oscillating magnetic field [11, 12], reciprocating motion by periodic magnetic field [13]). Apart from breaking the symmetry from the geometrical point of view, another strategy to overcome the Scallop Theorem and induce translational movement is introducing a physical boundary to break the spatial symmetry. Navigation on the surface of the blood vessels is advantageous because of decreased flow velocities. Inspired by leukocytes or neutrophils, which locomote in vascular channels along the vessel walls due to a relatively low flow velocity therein, magnetic surface walkers have been proposed for target delivery in confined microchannel environments [14-17]. Such locomotion can be achieved by magnetically activating a magnetic microrobot near a surface [18]. For example, crawling locomotion was achieved through Kresling origami-induced in-plane contraction caused by a magnetic actuation [19]. Stick-slip motion in the rectangular magnetic microrobot was induced by periodically varying magnetic fields [20]. An alternate form of locomotion was explored using a tumbling microrobot with a dumbbell structure with two oppositely polarized magnetic bell parts[21, 22]. The tumbling working mechanism, actuated with an alternating magnetic field, avoids the relative motion and constant contact against the surface, achieving effectiveness with their ability to access previously unreachable body areas.

To fabricate magnetic microrobots with desired architecture, various microfabrication techniques have been used, such as template-assisted electrodeposition[23], laser lithography[5, 11, 24, 25], glancing angle deposition[26, 27] and 3D printing[7, 9]. The magnetic section, such as Ni thin films and neodymium-iron-boron permanent magnets, was deposited during the fabrication. Among these fabrications, 3D printing provides a feasible approach to fabricating microrobots with predesigned shapes. In addition, several studies have utilized magnetic feedstock to produce high-performance bonded magnets using additive manufacturing. These studies demonstrate magnetic feedstock's potential in producing high-performance magnets with enhanced magnetic properties. The use of additive manufacturing techniques in combination with magnetic field alignment methods allows magnets with complex shapes and tailored magnetic properties, which can benefit a range of applications [28-30].

To actuate magnetic microrobots, a magnetic system usually consists of either an electromagnets [31-34] or permanent magnets as the source of the magnetic field [35-37]. Electromagnets-based magnetic actuation systems generate magnetic fields from flowing currents through coils. A typical electromagnet is formed by winding insulated copper wires around a ferromagnetic core, which concentrates and amplifies the magnetic field.

Triaxial circular Helmholtz coils are the most commonly used for actuating magnetic microrobots [26, 38]. While permanent magnets are easily obtainable and provide strong magnetic strength without a high current supply. The distribution and strength of the magnetic field depend on its geometrical shape and size.

Magnetic microrobots have great potential to deliver vehicles [39, 40] for magnetic nanoparticles (NPs)[41]. In our previous work, we have conducted both in vitro and in vivo experiments to study the application of superparamagnetic iron oxide (SPIO) NPs as drug carriers, which did not induce significant toxicity or inflammation in different cells and mice [42-45]. However, the rapid decay of magnetic field strength with distance from its source creates a significant challenge for controlling SPIO NPs[36, 45]. One fundamental limitation of the magnetic force-driven principle is that the external magnetic fields decrease roughly volumetrically in strength as distance increases between the magnetic objects and the area's source.

To improve the controllability of SPIO NPs, in this paper, we decorated SPIO NPs on the surface of magnetic-driven swimming microrobots. The microrobots are first 3D-printed and immersed in a water suspension of SPIO NPs for magnetic actuation. A custom magnet array with 12 permanent magnets and two DC motors creates a uniform rotating magnetic field inside the working space with magnetic strength of about 100 mT (Figure 1a). The difference in the orientation between the microrobot’s internal magnetization and that of a rotating magnetic field induces magnetic torque on the microrobot, making it tumble forward end-over-end (Figure 1b). Next, we show the motion of the microrobot under varying field rotational frequencies and demonstrate the ability of 2-dimensional controllability of the microrobot. Finally, we present a comprehensive dynamic model of the microrobot and its interactions with the magnetic fields. Such a model is necessary to understand the nature of the microrobot’s motion and thus can be used as a tool to optimize its geometry.

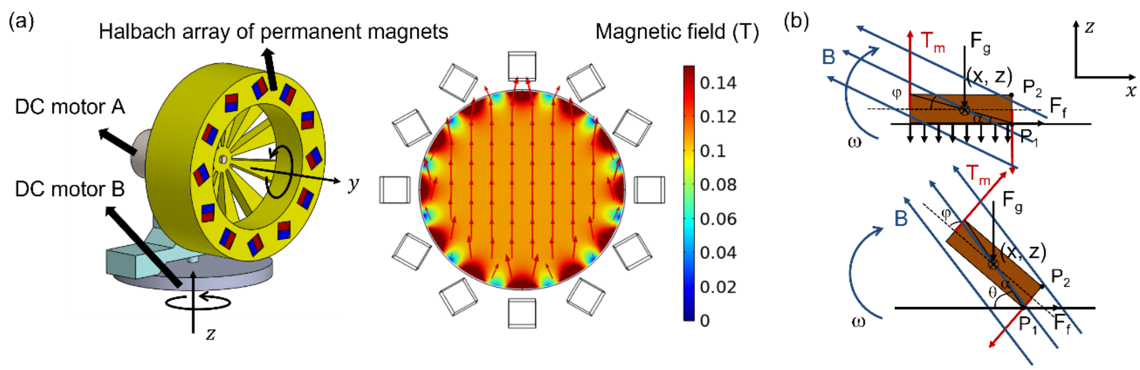

Figure 1. (a) The Schematic of the permanent magnet array design and the simulated 2D magnetic field profile shows the uniform magnetic field in the center. (b) Mechanism of the tumbling microrobot. The dashed lines represent the internal magnetic alignment, and its arrow represents the magnetic alignment's direction. The adhesive force is distributed uniformly over the surface area. The adhesive force is almost zero when the microrobot has line contact with the surface.

2. Design and Fabrication

The microrobot was 3D printed by using Stemaker™ Model D, which has a resolution of 10 microns in the X and Y directions and 100 microns in the Z direction, allowing for the creation of features as small as 10 microns in the X and Y directions and layer heights as small as 100 microns in the Z direction. However, achieving precise prints depends on the exposure time and light intensity. The 3D model was designed in Solidworks and sliced into a series of digital images. These images are then projected onto the photopolymerizable materials and loaded on a motorized stage. Areas illuminated by UV light (405 nm) crosslink within seconds while leaving the dark regions uncross-linked, forming a patterned layer in a specific polymerization plane. We used Poly (ethylene glycol) diacrylate (PEDGA Mn = 700 Da, Sigma) with the photoinitiator of 2% irgacure 819 Phenylbis (2,4,6-trimethyl benzoyl) phosphine oxide (Sigma). PEGDA is a synthetic polymer that is not biodegradable in the traditional sense. However, PEGDA can be biodegraded through other means, such as hydrolysis, which involves breaking down the polymer chain through a reaction with water. This process can occur over time, particularly under certain conditions such as exposure to heat or certain enzymes. Browning et al. [46] reported that the degradation mechanism of PEGDA hydrogels in vivo is primarily through hydrolysis of the end-group acrylate esters, which results in the cleavage of PEG chains from the hydrogel network. Stillman et al. [47] found that the PEDGA-based hydrogel nanoparticles degrade slowly in vitro, with more rapid degradation in vivo due to enzymes in the body. Besides, PEDGA displays essential features such as biocompatibility, biodegradability, and stealth, making it versatile for various bio-applications. For photopolymerization-based 3D printing, it is critical to determine the appropriate light exposure. Underexposure cannot photopolymerize the material, while overexposure may cause unwanted polymerization[48]. To achieve a high resolution and printability for the microrobot, 4 different light intensities (10%, 20%, 40%, and 60%) were chosen to print hollow cylinder and helix structures. We found that the structures swelled for the light intensity of 60%, suggesting overexposing. Thus, the print speed was set to 0.05 mm/s, and the light intensity was set to 40% for the following microrobots.

12 types of microrobots were designed and fabricated, including three series: 1) hollow series, 2) U shape series, and 3) complex series. In the hollow series, the performance of two different shapes, hollow cube, and hollow cylinder, and the effect of varying diameters of the hollow cylinder was compared. Four different shapes, square, rolling, long, and short U-shapes, were compared in the U-shape series. Finally, complex structures were further designed and fabricated to test the applicability of our theoretical model. To decorate PEDGA architecture with SPIO NPs for magnetic actuation, the microrobot was immersed in a water suspension of 200 mg/mL SPIO NPs (Ferrotec EMG 304) for 24 hours [9]. After coating, the color of the microrobots exhibits a consistent hue, which is considered acceptable in terms of uniformity for the 1 mm size range. The SPIO NPs in this paper are negatively charged, which makes them stable in aqueous solutions. The adsorption of SPIO NPs onto PEGDA surfaces is hypothesized to occur through a complex interplay of molecular interactions, including hydrogen bonds, electrostatic interactions, and van der Waals forces. Another possible mechanism is diffusion-controlled absorption, in which the SPIO NPs diffuse into the hydrogel matrix through the spaces between the polymer chains. Further research is needed to fully understand the mechanisms of SPIO NPs adsorption on PEGDA surfaces and to develop improved PEGDA-based magnetic microrobots. We conducted three measurements on both Hollow Cylinder 1 and Cylinder 2 before and after the coating process. The results

consistently show that the outer diameter of both structures increased by 10% after the coating.

2. Magnetic Propulsion

SPIO NPs become a single magnetic domain and exhibit high magnetic susceptibility properties in an external magnetic field, thereby introducing magnetization on microrobots. The magnetization orientation of microrobots influences their motion. The tumbling motion (rotation around its short axis) occurs near a surface under an external rotating magnetic field when a microrobot is magnetized along its long axis. However, when the microrobot is magnetized along its short axis, it rolls (rotates around its long axis) on the surface under the same applied rotating magnetic field. SPIO NPs are highly magnetic particles that exhibit unique behavior in the presence of an external magnetic field. When exposed to a magnetic field, SPIO NPs become magnetized and align themselves with the direction of the field. This property makes them a valuable magnetic material to create magnetic microrobots without needing pre-magnetization along different axes.

The tumbling motion of the microrobot discussed in this paper is achieved by providing rotating magnetic fields from the magnetic applicator in Figure 1a. A Halbach array of 12 magnets (NdFeB, grade N52, core strength of 1.48 T, dimensions 12.7 × 12.7 × 25.4 mm, K&J Magnetics, Inc.) was designed to generate a uniform magnetic field inside the center. By rotating this Halbach array through a DC motor (motor A), a uniform magnetic field can be generated with a magnetic strength of about 100 mT as simulated by COMSOL Multiphysics. In addition, the bottom of the applicator was attached to another DC motor (motor B), which enabled this magnetic field to control the forward direction of the tumbling microrobot.

To simulate the dynamics of the swimming microrobot, we assume it is an isotropic rectilinear solid and restrict modeling to a side-view of the microrobot in the *x*-*z* plane, shown in Figure 1b. The microrobot's position (x, z) is taken at its center of mass (COM) and has an orientation angle θ measured clockwise from the ground, a distance r from its COM to a corner, and an angle $\alpha = \tan^{-1}\frac{D}{L}$ determined from geometry. As the magnetic applicator rotates, the driving torque is generated, lifting the microrobot to tumble. The microrobot must follow the rotating magnetic field before another tumble is possible. The translational velocity of the microrobot grows with the rotating frequency (ω) of the magnetic field until a step-out frequency is reached. Beyond this step-out frequency, the available magnetic torque is insufficient to keep the microrobot tumbling to follow the rotating magnetic field.

The microrobot performs periodic tumbling motions. The microrobot is first assumed pinned to the point P_1, where $0 \leq \theta \leq \frac{\pi}{2}$, then is pinned to the point P_2, when. Due to the uniformity of the applied rotating magnetic field, a negligible magnetic force was exerted on the microrobot. Assuming there is no sliding motion, the governing equation of the tumbling microrobot can be expressed as:

$$I\ddot{\theta} = T_m - \tau_d - F_g r \times \cos(\theta + \alpha) - F_a \frac{L}{2} \quad (1)$$

The magnetic torque applied on the microrobot $T_m = V_m|M||B| \sin\varphi$, where $\varphi = \omega t - \theta$ is the magnetic alignment offset angle. The drag torque per unit length L of a cylinder rotating close to a wall is given by[49], $\frac{\tau_d}{L} = \frac{4\pi u_d \dot{\theta} r^2}{\sqrt{1-k^2}}$, where $k = \frac{r}{r+d_0}$, d_0 depicts the gap distance between the microrobot and surface and u_d is the dynamic viscosity of water. The volumetric vertical force of the microrobot $F_g = \rho_{spio} g V_m + \rho_{PEGDA} g V - \rho_{water} g (V_m + V)$ is the combined action of the weight of the microrobot and its buoyancy. Here, V is the volume of the microrobot without SPIO NPs coating, ρ_{spio}, ρ_{PEGDA}, ρ_{water} are the density of the SPIO NPs, PEGDA, and water, respectively. $F_a = C_a S$ is the adhesive force between the microrobot and the surface when it rests, where C_a is the coefficient of adhesive force, S is the contact area. Based on the governing equation, the design of a microrobot determines its tumbling motion. A smaller moment of inertia will result in a faster rotation for a given torque, meaning that a microrobot with a smaller moment of inertia will require less torque to achieve the same angular acceleration than a structure with a larger moment of inertia. For a uniform structure, the moment of inertia is directly proportional to its length. Therefore, a longer microrobot will have a more significant moment of inertia than a shorter one, assuming they have the same mass and uniform mass distribution. However, a longer length will also result in enormous drag torque, requiring more magnetic torque to lift it. The equation can be numerically solved by using MATLAB software.

Table 1. Parameters for theoretical analysis

Parameters	Symbol	Value
Radius of SPIO NP	R	5 [nm]
Volume of SPIO NP	V_{SPIO}	5.23×10^{-25} [m^3]
Density of SPIO NP	ρ_{SPIO}	5240 [kg/m^3]
Single SPIO mass	m_{SPIO}	2.74×10^{-21} [kg]
Density of PEGDA	ρ_{PEGDA}	1120 [kg/m^3]
Density of water	ρ_{water}	1000 [kg/m^3]
Rotating magnetic field	B	0.1 [T]
Magnetization of SPIO	M	21936.75 [A/m]
Coefficient of adhesive force	C_a	1.19 [N/m^2]
Number of SPIO NPs in microrobot	n	$S_0/(\pi R^2)$
Magnetic part volume	V_m	$n \times V_{SPIO}$ [m^3]
Total mass	m	$m_0 + n \times m_{SPIO}$ [kg]
Moment of inertia	I	$I_0/m_0 \times m$ [kg.m^2]

Table 1 shows the parameters used in the theoretical analysis of the motion of the microrobots. The subscript of 0 means the properties of the microrobot before coating SPIO NPs. Figure 2a displays several frames from one 60 frames per second experimental video of Helix 2 in the *x*-*y* plane exhibiting tumbling motion when actuated by a rotating magnetic field at 0.42 Hz. Figure 2b depicts the simulated motion (rotation degree) of Helix 2 in the *x*-*z* plane.

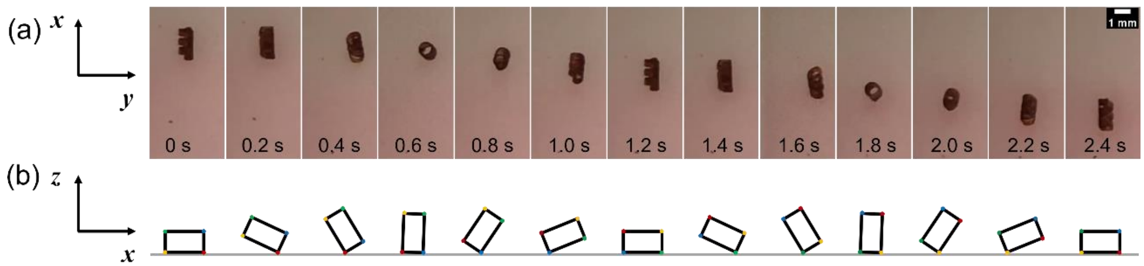

Figure 2. Frames extracted from the video recording of Helix 2 under the rotating magnetic field at 0.42 Hz, compared to the simulated results. (a) The microrobot initially rests on the surface. When the magnetic field rotates, the microrobot tumbles to align the magnetic field. The contact points keep changing, and the microrobot moves forward. (b) The simulated responses of the rotation degree. The contact points change from red, blue, and green to yellow.

4 Experimental Studies

To evaluate the performance of microrobots and calculate their translational velocity, the microrobot was detected using OpenCV and Python. We first removed the noise in the video with a Gaussian filter. This step slightly smoothed the images to reduce the effects of obvious noise on the edge detector. And then, the edge of the microrobot was detected by the Canny edge detection algorithm. Thus, the microrobot's translational speed and offset degree can be calculated. The real-time speed and offset degree of Helix 2 under the rotating magnetic field at 3.2 Hz (Figure 3) indicated that it translated forward with an approximately uniform speed.

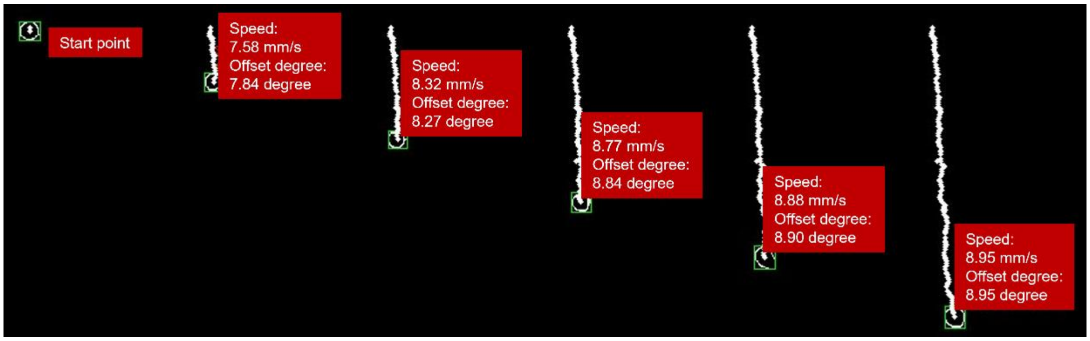

Figure 3. Frames extracted from the video after detecting the motion of Helix 2 under the rotating magnetic field at 3.2 Hz with OpenCV (time step = 0.5 s).

The average translational speeds of the hollow series, U-shape series, and other shape series microrobots under varying field rotational frequencies were studied. Table 2 lists different microrobot shapes' maximum translational speeds and step-out frequencies. For the hollow series microrobots, a maximum translational speed of 17.87 mm/s was measured for Hollow Cube at the frequency of 5.26 Hz, and 10.40 mm/s for Hollow Cylinder 1 at 4.50 Hz, 16.84 mm/s for Hollow Cylinder 2 at 8.00 Hz, 12.62 mm/s for Hollow Cylinder 3 at 6.60 Hz. The theoretical results agree well with the experimental results, especially for the Hollow Cube microrobot. The reason could be that the microrobot was treated as an isotropic rectilinear solid in the theoretical model, and the other shape was not considered. Among these 12 shapes of microrobots, we found that the microrobots with equal length, width, and depth, such as Hollow Cube, Hollow,

Table 2. The maximum speed and frequency for different shapes of microrobots

Microrobots	Maximum speed (mm/s)	Step-out frequency (Hz)
Hollow series		
Hollow Cube	17.87	5.26
Hollow Cylinder 1	10.40	4.50
Hollow Cylinder 2	16.84	8.00
Hollow Cylinder 3	12.62	6.60
U series		
Square U	17.29	7.64
Rolling U	5.09	1.59
Short U	13.52	5.21
Long U	15.94	4.01
Other shape series		
Helix 1	9.04	3.95
Helix 2	7.95	3.00
Z shape	13.87	5.11
2 Hollow Cylinder	14.12	4.41

Cylinder 2, and Square U, had better performance. Since the entire surface of microrobots is coated with SPIO NPs, some areas are perpendicular to the magnetic field and generate resisting torque during the tumbling. Thus, theoretical analysis of some structures still suggested that the speed of microrobots would continue to increase as the rotating frequency increases. Overall, the theoretical model can predict the motion of the tumbling microrobot of different shapes, thus guiding the design of microrobots.

To demonstrate the two-dimensional controllability of the microrobot, Helix 2 was driven on a 3D-printed Circle of Willis[36]. The microrobot's motion was confined to the *x*-*y* plane. Linear propulsion is achieved by a rotating magnetic field driven by the DC motor A, while the direction in the *x*-*y* plane is controlled by the motor B. By simultaneously rotating the magnetic applicator about the *y* and *z* axes for the tumbling and turning of the microrobot respectively, the microrobot can translate in 2 dimensions. It was shown that Helix 2 can be transported through either ACA or MCA under the rotating frequency of 0.5 Hz.

Currently, the controllability of small-scale robots is limited in stagnant fluidic environments. The drag force of substantial fluidic flows may disrupt the propulsion capability and disturb the motion control of a microrobot, resulting in negative net motion or uncontrolled locomotion in the viscous biofluids[2]. To date, it is still unclear how to make microrobots resist the variable flow rate. Without overcoming this problem, the microrobots could not pass through the blood vessels in a controllable manner to arrive at the targeted location. Here, we conducted a simulation in COMSOL Multiphysics to test the motion of the tumbling microrobot under a flow rate of 0.062 m/s (the general blood flow rate of the adult mice)[50]. A clockwise or counterclockwise rotating magnetic field affects the speed of the microrobot (acceleration or deceleration) compared to the case where no magnetic field is applied.

5. Conclusion

In this study, the performance and modeling of a permanent magnet array of actuated tumbling microrobots have been demonstrated. The microrobot was subjected to a uniform rotating magnetic field in the experiment and simulation, which induced a tumbling motion over the surface. The translational speed of tumbling microrobots was presented versus rotating frequency for 12 shapes of microrobots. The dynamics model of the microrobot has been demonstrated in this study, which can be used to predict the behavior of tumbling microrobots with different shapes and serve as a useful tool to guide structural design. The simulation can predict the step-out frequency for the helix structure microrobot. For some complex structures, the theoretical model can generally expect the overall trend of the microrobot's behavior but overestimate its step-out frequency. Errors are likely due to the slippage of microrobots in practice under a higher rotating field frequency. For practical use, it is desirable to investigate the behavior of microrobots in vascular environments rather than steering in stagnant liquids. Our simulated results demonstrated that the tumbling microrobot could accelerate or decelerate in the bloodstream, which was beneficial for controlled active drug release.

Future works will include incorporating more accurate friction and adhesion (obtained from experiments) model and considering the slippage of microrobots into the theoretical model. In addition, an autonomous feedback control system will also be investigated, which can lead to the precise delivery of the microrobot to the final target destination. The motion of the microrobot in a flow biofluid environment will also be examined.

Acknowledgments

This work was kindly supported by the United States National Science Foundation (NSF) (Award # CMMI 1851635 and # ECCS 2021081).

References

[1] E.M. Purcell, Life at low Reynolds number, Am. J. Phys., 45 (1977) 3-11.
[2] M. Sitti, H. Ceylan, W. Hu, J. Giltinan, M. Turan, S. Yim, E. Diller, Biomedical Applications of Untethered Mobile Milli/Microrobots, Proc. IEEE, 103 (2015) 205-224.
[3] D.-i. Kim, S. Song, S. Jang, G. Kim, J. Lee, Y. Lee, S. Park, Untethered gripper-type hydrogel millirobot actuated by electric field and magnetic field, Smart Mater. Struct., 29 (2020) 085024.
[4] S. Mohanty, Q. Jin, G.P. Furtado, A. Ghosh, G. Pahapale, I.S.M. Khalil, D.H. Gracias, S. Misra, Bidirectional Propulsion of Arc-Shaped Microswimmers Driven by Precessing Magnetic Fields, Advanced Intelligent Systems, 2 (2020) 2000064.
[5] C. Xin, D. Jin, Y. Hu, L. Yang, R. Li, L. Wang, Z. Ren, D. Wang, S. Ji, K. Hu, D. Pan, H. Wu, W. Zhu, Z. Shen, Y. Wang, J. Li, L. Zhang, D. Wu, J. Chu, Environmentally Adaptive Shape-Morphing Microrobots for Localized Cancer Cell Treatment, ACS Nano, (2021).
[6] U. Bozuyuk, O. Yasa, I.C. Yasa, H. Ceylan, S. Kizilel, M. Sitti, Light-Triggered Drug Release from 3D-Printed Magnetic Chitosan Microswimmers, ACS Nano, 12 (2018) 9617-9625.
[7] H. Ceylan, I.C. Yasa, O. Yasa, A.F. Tabak, J. Giltinan, M. Sitti, 3D-Printed Biodegradable Microswimmer for Theranostic Cargo Delivery and Release, ACS Nano, 13 (2019) 3353-3362.
[8] J.J. Abbott, K.E. Peyer, M.C. Lagomarsino, L. Zhang, L. Dong, I.K. Kaliakatsos, B.J. Nelson, How Should Microrobots Swim?, The International Journal of Robotics Research, 28 (2009) 1434-1447.
[9] X. Wang, X.-H. Qin, C. Hu, A. Terzopoulou, X.-Z. Chen, T.-Y. Huang, K. Maniura-Weber, S. Pané, B.J. Nelson, 3D Printed Enzymatically Biodegradable Soft Helical Microswimmers, Advanced Functional Materials, 28 (2018) 1804107.
[10] D. Son, M.C. Ugurlu, M. Sitti, Permanent magnet array-driven navigation of wireless millirobots inside soft tissues, Science Advances, 7 (2021) eabi8932.
[11] P. Liao, J. Li, S. Zhang, D. Sun, A Fish-Like Magnetically Propelled Microswimmer Fabricated by 3D Laser Lithography, in: 2018 IEEE International Conference on Robotics and Automation (ICRA), 2018, pp. 3581-3586.
[12] B. Jang, E. Gutman, N. Stucki, B.F. Seitz, P.D. Wendel-García, T. Newton, J. Pokki, O. Ergeneman, S. Pané, Y. Or, B.J. Nelson, Undulatory Locomotion of Magnetic Multilink Nanoswimmers, Nano Letters, 15 (2015) 4829-4833.
[13] T. Li, J. Li, H. Zhang, X. Chang, W. Song, Y. Hu, G. Shao, E. Sandraz, G. Zhang, L. Li, J. Wang, Magnetically Propelled Fish-Like Nanoswimmers, Small, 12 (2016) 6098-6105.
[14] Y. Alapan, U. Bozuyuk, P. Erkoc, A.C. Karacakol, M. Sitti, Multifunctional surface microrollers for targeted cargo delivery in physiological blood flow, Science Robotics, 5 (2020) eaba5726.
[15] Z. Lin, X. Fan, M. Sun, C. Gao, Q. He, H. Xie, Magnetically Actuated Peanut Colloid Motors for Cell Manipulation and Patterning, ACS Nano, 12 (2018) 2539-2545.
[16] W. Chen, X. Fan, M. Sun, H. Xie, The cube-shaped hematite microrobot for biomedical application, Mechatronics, 74 (2021) 102498.
[17] D. Ahmed, T. Baasch, N. Blondel, N. Läubli, J. Dual, B.J. Nelson, Neutrophil-inspired propulsion in a combined acoustic and magnetic field, Nature Communications, 8 (2017) 770.
[18] W.-Z. Fang, S. Ham, R. Qiao, W.-Q. Tao, Magnetic Actuation of Surface Walkers: The Effects of Confinement and Inertia, Langmuir, 36 (2020) 7046-7055.
[19] Q. Ze, S. Wu, J. Nishikawa, J. Dai, Y. Sun, S. Leanza, C. Zemelka, L.S. Novelino, G.H. Paulino, R.R. Zhao, Soft robotic origami crawler, Science Advances, 8 (2022) eabm7834.
[20] C. Pawashe, S. Floyd, M. Sitti, Modeling and Experimental Characterization of an Untethered Magnetic Micro-Robot, The International Journal of Robotics Research, 28 (2009) 1077-1094.
[21] W. Jing, N. Pagano, D.J. Cappelleri, A novel micro-scale magnetic tumbling microrobot, Journal of Micro-Bio Robotics, 8 (2013) 1-12.
[22] C. Bi, M. Guix, B.V. Johnson, W. Jing, D.J. Cappelleri, Design of Microscale Magnetic Tumbling Robots for Locomotion in Multiple Environments and Complex Terrains, Micromachines, 9 (2018) 68.

[23] B. Jang, A. Hong, C. Alcantara, G. Chatzipirpiridis, X. Martí, E. Pellicer, J. Sort, Y. Harduf, Y. Or, B.J. Nelson, S. Pané, Programmable Locomotion Mechanisms of Nanowires with Semihard Magnetic Properties Near a Surface Boundary, ACS Applied Materials & Interfaces, 11 (2019) 3214-3223.
[24] M. Suter, L. Zhang, E.C. Siringil, C. Peters, T. Luehmann, O. Ergeneman, K.E. Peyer, B.J. Nelson, C. Hierold, Superparamagnetic microrobots: fabrication by two-photon polymerization and biocompatibility, Biomedical Microdevices, 15 (2013) 997-1003.
[25] H.C.M. Sun, P. Liao, T. Wei, L. Zhang, D. Sun, Magnetically Powered Biodegradable Microswimmers, Micromachines, 11 (2020) 404.
[26] A. Ghosh, P. Fischer, Controlled Propulsion of Artificial Magnetic Nanostructured Propellers, Nano Letters, 9 (2009) 2243-2245.
[27] H.-W. Huang, M.S. Sakar, A.J. Petruska, S. Pané, B.J. Nelson, Soft micromachines with programmable motility and morphology, Nature Communications, 7 (2016) 12263.
[28] A.P. Taylor, J. Izquierdo Reyes, L.F. Velásquez-García, Compact, magnetically actuated, additively manufactured pumps for liquids and gases, Journal of Physics D: Applied Physics, 53 (2020) 355002.
[29] A.P. Taylor, C.V. Cuervo, D.P. Arnold, L.F. Velásquez-García, Fully 3D-Printed, Monolithic, Mini Magnetic Actuators for Low-Cost, Compact Systems, J. Mricomech. Syst., 28 (2019) 481-493.
[30] L. Li, A. Tirado, I.C. Nlebedim, O. Rios, B. Post, V. Kunc, R.R. Lowden, E. Lara-Curzio, R. Fredette, J. Ormerod, T.A. Lograsso, M.P. Paranthaman, Big Area Additive Manufacturing of High Performance Bonded NdFeB Magnets, Sci. Rep., 6 (2016) 36212.
[31] M.P. Kummer, J.J. Abbott, B.E. Kratochvil, R. Borer, A. Sengul, B.J. Nelson, OctoMag: An Electromagnetic System for 5-DOF Wireless Micromanipulation, IEEE Transactions on Robotics, 26 (2010) 1006-1017.
[32] S. Jeon, A.K. Hoshiar, K. Kim, S. Lee, E. Kim, S.L. Lee, J.-y. Kim, B.J. Nelson, H.-J. Cha, B.-J. Yi, H. Choi, A Magnetically Controlled Soft Microrobot Steering a Guidewire in a Three-Dimensional Phantom Vascular Network, Soft Robotics, 6 (2019) 54-68.
[33] S. Schuerle, S. Erni, M. Flink, B.E. Kratochvil, B.J. Nelson, Three-Dimensional Magnetic Manipulation of Micro- and Nanostructures for Applications in Life Sciences, IEEE Trans. Magn., 49 (2013) 321-330.
[34] J. Yu, D. Jin, K.-F. Chan, Q. Wang, K. Yuan, L. Zhang, Active generation and magnetic actuation of microrobotic swarms in bio-fluids, Nature Communications, 10 (2019) 5631.
[35] K.E. Peyer, L. Zhang, B.J. Nelson, Bio-inspired magnetic swimming microrobots for biomedical applications, Nanoscale, 5 (2013) 1259-1272.
[36] J. Chen, Y. Wang, Personalized dynamic transport of magnetic nanorobots inside the brain vasculature, Nanotechnology, 31 (2020) 495706.
[37] O. Baun, P. Blümler, Permanent magnet system to guide superparamagnetic particles, Journal of Magnetism and Magnetic Materials, 439 (2017) 294-304.
[38] P. Fischer, A. Ghosh, Magnetically actuated propulsion at low Reynolds numbers: towards nanoscale control, Nanoscale, 3 (2011) 557-563.
[39] S. Kim, F. Qiu, S. Kim, A. Ghanbari, C. Moon, L. Zhang, B.J. Nelson, H. Choi, Fabrication and characterization of magnetic microrobots for three-dimensional cell culture and targeted transportation, Adv Mater, 25 (2013) 5863-5868.
[40] S. Lee, S. Kim, S. Kim, J.-Y. Kim, C. Moon, B.J. Nelson, H. Choi, A Capsule-Type Microrobot with Pick-and-Drop Motion for Targeted Drug and Cell Delivery, Advanced Healthcare Materials, 7 (2018) 1700985.
[41] Wahajuddin, S. Arora, Superparamagnetic iron oxide nanoparticles: magnetic nanoplatforms as drug carriers, Int J Nanomedicine, 7 (2012) 3445-3471.
[42] M. Yuan, E.A. Bancroft, J. Chen, R. Srinivasan, Y. Wang, Magnetic Fields and Magnetically Stimulated Gold-Coated Superparamagnetic Iron Oxide Nanoparticles Differentially Modulate L-Type Voltage-Gated Calcium Channel Activity in Midbrain Neurons, ACS Applied Nano Materials, 5 (2022) 205-215.
[43] M. Yuan, Y. Wang, Y.-X. Qin, SPIO-Au core–shell nanoparticles for promoting osteogenic differentiation of MC3T3-E1 cells: Concentration-dependence study, Journal of Biomedical Materials Research Part A, 105 (2017) 3350-3359.
[44] M. Yuan, Y. Wang, Y.-X. Qin, Promoting neuroregeneration by applying dynamic magnetic fields to a novel nanomedicine: Superparamagnetic iron oxide (SPIO)-gold nanoparticles bounded with nerve growth factor (NGF), Nanomedicine: Nanotechnology, Biology and Medicine, 14 (2018) 1337-1347.

[45] J. Chen, M. Yuan, C.A. Madison, S. Eitan, Y. Wang, Blood-brain barrier crossing using magnetic stimulated nanoparticles, Journal of Controlled Release, 345 (2022) 557-571.
[46] M.B. Browning, S.N. Cereceres, P.T. Luong, E.M. Cosgriff-Hernandez, Determination of the in vivo degradation mechanism of PEGDA hydrogels, Journal of Biomedical Materials Research Part A, 102 (2014) 4244-4251.
[47] Z. Stillman, B.M. Jarai, N. Raman, P. Patel, C.A. Fromen, Degradation profiles of poly(ethylene glycol)diacrylate (PEGDA)-based hydrogel nanoparticles, Polymer Chemistry, 11 (2020) 568-580.
[48] S. You, P. Wang, J. Schimelman, H.H. Hwang, S. Chen, High-fidelity 3D Printing using Flashing Photopolymerization, Additive manufacturing, 30 (2019) 100834.
[49] R. Pieters, H.W. Tung, S. Charreyron, D.F. Sargent, B.J. Nelson, RodBot: A rolling microrobot for micromanipulation, in: 2015 IEEE International Conference on Robotics and Automation (ICRA), 2015, pp. 4042-4047.
[50] G. Yankova, D. Tur, D. Parshin, A. Cherevko, A. Akulov, Cerebral arterial architectonics and CFD simulation in mice with type 1 diabetes mellitus of different duration, Sci. Rep., 11 (2021) 3969.